Journal of Materials Chemistry A

Accepted Manuscript

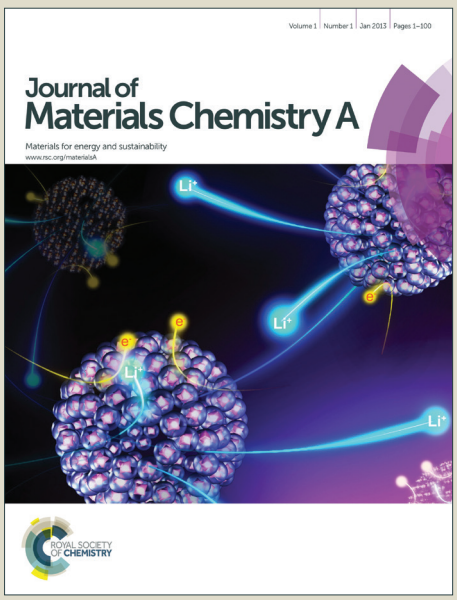

ROYAL SOCIETY OF CHEMISTRY

www.rsc.org/materialsA

Graphical abstract

Experimental and computed studies for $(La_{1-x}Sr_x)CoO_{3-\delta}$ show the correlation among the mixed ionic–electronic conduction, crystal, local, and electrical structures. The change of spin states estimated by pre-edge analysis was observed at x=0.15 to occur concomitantly the Metal-Insulator transition.

ARTICLE TYPE
www. rsc.org/xxxxxx | XXXXXXXX

Correlation between structure and mixed ionic–electronic conduction mechanism for $(La_{1-x}Sr_x)CoO_{3-\delta}$ using synchrotron X-ray analysis and first principles calculations

Takanori Itoh,*[a]‡ Manabu Inukai,[b] Naoto Kitamura,[a] Naoya Ishida,[a] Yasushi Idemoto,[a] Takashi Yamamoto,[c]

Received Xth XXXXXXXXXX 20XX, Accepted Xth XXXXXXXXX 20XX
First published on the web Xth XXXXXXXXXX 200X
DOI: 10.1039/b000000x

The mechanism of mixed ionic–electronic conduction (MIEC) for $(La_{1-x}Sr_x)CoO_{3-\delta}$ (LSC) ($x = 0.00 - 0.50$) was investigated by the experimental as well as the theoretical studies including Rietveld refinements, Maximum Entropy Method (MEM) analysis, X-ray absorption spectroscopy, and first principles calculations (FPC). The correlations among MIEC, structure parameters, *i.e*, the bond length and the bond angle, electron density, and the spin configuration were discussed from the practical results. Moreover, these correlations were verified by FPC, and interpreted by the band structure and the total energy of LSC. The electronic conductivity was affected by Co–O–Co bond angle, electron density, and the spin state. In particular, the spin transition from the low spin state to the high spin one was accompanied by the cross-over from semiconductor to metallic at $x = 0.15$. Concerning the oxide ion diffusion, LSC has large anisotropic atomic displacement parameters of the oxide ion sites, in the vertical direction of Co–O bond, which associate with the high oxide ion diffusion. The total energy of LSC during migrating the oxide ion was also calculated with varying Sr content, lattice parameters, and symmetry by using FPC. Consequently, the symmetry of LSC is more effective to reduce the activation energy of the oxide ion diffusion than Sr content and lattice parameters.

1 Introduction

Perovskite oxides are the focus of intense interest for possessing various properties in electrical conductivity, ion diffusion, catalysis, thermoelectric performance, magnetism, *etc*[1,2]. Specifically, perovskite oxides are promising materials used in electrochemical applications, such as the solid oxide fuel cells (SOFCs), where they were used in the electrode, oxygen pumps, oxygen sensors, and oxygen separation membranes[3–5]. In the electrochemical applications, performance of them is dominated by mixed ionic–electronic conduction (MIEC) of perovskite oxides. Conduction in many perovskite oxides occurs due to the electrons and the oxide ions; it is also influenced by various parameters such as structural parameters, composition elements, valence states, and oxide ion vacancies.

For perovskites, lanthanum cobaltite perovskites are widely used as the cathode materials of SOFCs because of their higher MIEC than other perovskite oxides at medium operating temperatures[3,6–9]. In particular, $(La_{1-x}Sr_x)CoO_{3-\delta}$ (LSC) has been widely investigated from various viewpoints. As for MIEC, the electronic conductivity (σ_e) and oxide ion diffusion coefficient ($D_{O^{2-}}$) have been extensively studied for LSC.

Concerning a dependence of σ_e on x, the phase for $x < 0.15$ is semiconductive; whereas, that for $x \geq 0.15$ is metallic[10–12]. The Metal–Insulator (M–I) transition is related to the crystal structure of LSC[10,13]. The electronic structure of LSC, which is deeply associated with σ_e, have been investigated by first principle calculations (FPC) and X-ray absorption spectra (XAS). It was reported that the hybridization enhanced between the Co 3*d* and O 2*p* band by FPC for LSC[14,15]. Kozuka et al. presented that the higher mobility of electrons in LSC arose from the transition to a high spin state by using FPC[16]. In the available literature for studies of LSC, XAS has been widely used for studying the band structure and the spin configuration of Co atom. Toulemonde et al. recorded Co *K*-edge X-ray absorption near-edge structure (XANES) for $LaCoO_3$, and proposed that the spin state was a mixed low spin and intermediate spin[17].

In the case of $D_{O^{2-}}$, oxide ion vacancies, and oxygen

[a] *Department of Pure and Applied Chemistry, Faculty of Science and Technology, Tokyo University of Science, Noda City, Chiba 278-8510, Japan*
[b] *Department of Material Science and Engineering, Faculty of Engineering, Nagoya Institute of Technology, Gokiso-cho, Showa-ku, Nagoya 466-8555, Japan.*
[c] *Department of Mathematical and Material Sciences, Faculty of Integrated Arts and Sciences, The University of Tokushima, Tokushima 770-8502, Japan.*
‡ Present address: AGCSeimicemical Co., LTD. Hirai, Kashima, Ibaraki, 314-0012, Japan, Fax: +81 299 84 0217; Tel: +81 299 84 0808; E-mail: takanori.itoh@agc.com
† Electronic Supplementary Information (ESI) available: Supporting tables, referenced in the text. See DOI: 10.1039/b000000x/

nonstoichiometry have been studied in details by iodimetry, thermo gravimetry (TG), and conductivity measurements, variously and widely. Oxygen vacancies increase with increase in Sr content x[10,16,18]. Mizusaki et al. studied the oxygen nonstoichiometry, depended on temperature and oxygen partial pressure, by TG in detail[19]. Berenov et al. studied that $D_{O^{2-}}$ increased with increase in x by using Secondary Ion Mass Spectroscopy[20]. Islam estimated oxide ion transport mechanism in perovskites by computing modeling[21].

Most of studies for LSC, however, did not discuss the correlations among MIEC, crystal structure parameters, electron densities, band structures, and spin configurations, quantitatively. In this work, we discuss these correlations in detail on a semiquantitative level. The crystal structure parameters, *i.e.*, bond length, bond angle, and atomic displacement parameter are estimated by Rietveld refinements using synchrotron X-ray diffraction (SR-XRD) data, and the experimental electron density is calculated by the Maximum Entropy Method (MEM) analysis using results of Rietveld refinements. The band structures and spin configurations are studied by using the pre–edge in XANES. In addition, the correlation between structural parameters and MIEC is verified by using FPC. We present the correlation among MIEC mechanism, structural parameters, electron densities, spin configuration, and band structures, empirically and theoretically.

2 Experimental

2.1 Sample preparation and characterization

$(La_{1-x}Sr_x)CoO_{3-\delta}$ (LSC) ($x = 0.00 - 0.50$ with 0.05 steps) samples were prepared by the solid state reaction. Appropriate amount of La_2O_3 (Furuuchi Chemicals, Japan $>$ 99.9 %), $SrCO_3$ (Honjo Chemical, Japan $>$ 99.99 %), $2CoCO_3{\cdot}3Co(OH)_2{\cdot}4H_2O$ (Kanto Chemicals, Japan $>$ 99.9 %) were dispersed in AK-225AE (AGC, Japan) as an organic solvent. The starting materials were mixed homogenously by the planetary zirconia ball milling for 12 h. The slurry was dried at 393 K in an oven, and the powder was calcinated in air at 673K for 6 h, 873 K for 6 h, then grounded, and followed by another calcination at 1473 K for 6 h. The annealing procedure was performed at 673 K for 48 h in air, and the slow cooling rate allowed the sample to remove the oxide ion vacancies. X-ray diffraction (XRD) measurements (RINT2200V, Rigaku Corp., Japan) of the compound confirmed that the samples were consisted of a single phase. The metal elemental composition was determined by inductively coupled plasma (ICP) atomic emission spectroscopy (SPS-1700 HVR, SII Nanotechnology Inc., Japan), using the spectral wavelengths of 408.6 nm for La, 407.8 nm for Sr, and 228.6 nm for Co. The average Co valence was determined by potentiometric-titration measurements (AT-500N, KEM, Japan) using Mohr's salt[22]. Oxygen content and oxide ion site occupancy were calculated from the average Co valence based on the charge neutral principle with La^{3+}, Sr^{2+}, and O^{2-}.

2.2 Structural parameters and electron density

Synchrotron X-ray diffraction (SR-XRD) experiments were carried out using a large Debye-Scherrer camera installed at BL19B2 beamline in SPring-8 (Hyogo, Japan)[23]. SR-XRD data was taken for the 2θ range of values $5^\circ - 40^\circ$ with a step interval of 0.01° with X-ray wavelength of 0.350334 Å, which was determined by calibrating a NIST CeO_2 standard sample. Diffraction data of LSC were analyzed by Rietveld refinement technique using the program RIETAN-FP[24]. SR-XRD data were analyzed using the modified split pseudo-Voigt function proposed by Izumi and Ikeda[25]. Maximum Entropy Method (MEM) analysis was carried out using Dysnomia program, and performed on a unit cell of LSC which was distributed over $60 \times 60 \times 144$ pixels. MEM analysis used structure parameters obtained from Rietveld refinements for all samples[26,27]. Corresponding crystal structures and electron densities were visualized by using the software package VESTA[28].

2.3 X-ray absorption spectra

X-ray absorption (XAS) experiments at Co *K*-edge were performed at BL14B2 beamline with the bending magnet of SPring-8 (Hyogo, Japan) at room temperature. A Si(111) double-crystal monochromator was used for energy selection. X-ray intensities for incident and transmitted beams were monitored using ionization chambers filled with a helium–nitrogen mixture (50/50 %) and a nitrogen–argon mixture (85/15 %), respectively. The statistical error of energy, estimated from 30 scans, was 0.022 eV at Co *K*-edge energy. For XAS measurements, LSC samples were mixed with a suitable amount of boron nitride. The energy calibration was carried out to be 7709 eV at the half normalized absorption for Co *K*-edge XANES spectrum of pure Co foil with a 4 μm thickness. All XAS data were normalized using software Athena in IFEFFIT 1.2.11[29,30]. A Hill function was used as a background function at the Co pre–edge.

2.4 First principles calculations

Calculations for density of states (DOS) and the total energy (E_{total}) of LSC during migrating oxide ion were performed by first principles calculations (FPC) using the density functional theory on the basis of the full potential augmented plane wave plus local orbital (APW+lo) method as implemented in WIEN2k code[31]. The generalized gradient approximation (GGA) in the scheme of Perdue Bruke Ermzerhof with an effective Coulomb parameter (U_{eff}), *i.e.*, GGA+U, was used for

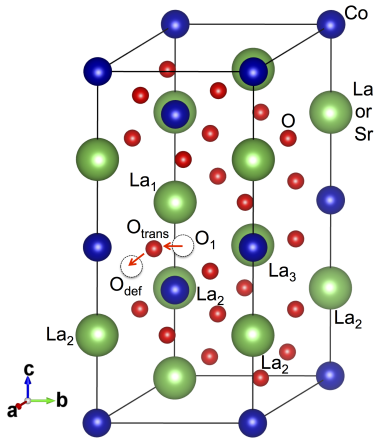

Fig. 1 Structure model with space group $P1$ for first principles calculating the total energy during migrating oxide ion. The initial oxide ion deficiency site (O_{def}), The oxide ion site (O_{trans}) with the lowest total energy in the oxide ion path from O_1 to O_{def}.

the exchange correlation energy[32]. In APW + lo method, we used the following electron configurations for the core state: [Kr]$4d^{10}$ for La, [Ar]$3d^{10}$ for Sr, [Ne]$3s^2$ for Co, and [He] for O. The muffin-tin radii were chosen to be 2.48, 2.37, 1.96, and 1.69 au for La, Sr, Co, and O, respectively. The summation in the Brillouin zone was performed using 1000 $k-$points. The cutoff parameter was set to $R_{mt}K_{max} = 7$. We chose a $U_{eff} = 7$ eV, which was referred from Korotin et al., for Co atom[33]. The space group $R\bar{3}c$ and structural parameters, *i.e.*, lattice parameters and bond angles, estimated by Rietveld refinements were used in FPC for estimating DOS. Table S1 lists the conditions of FPC for DOS†.

The structure in Fig. 1 with space group $P1$ was used for calculating E_{total} of LSC during migrating the oxide ion, and the activation energy (E_a) of oxide ion diffusion by FPC. We estimated the total initial energy (E_{ini}) of LSC with the oxide ion vacancy; The deficiency site was O_{def} site in Fig. 1 at the initial state. The transition energy (E_{trans}) of LSC with O_{trans} site was the lowest total energy in the oxide ion path from O_1 to O_{def} in Fig. 1. E_a was defined to the following equation:

$$E_a = E_{trans} - E_{ini}. \quad (1)$$

We used parameters for FPC such as lattice parameter and bond angles estimated by Rietveld refinements, and Sr content. In some cases of FPC, La_1, La_2, and La_3 atoms were substituted by Sr atom in Fig. 1. Table S2 gives the condition of FPC for discussing the oxide ion diffusion†.

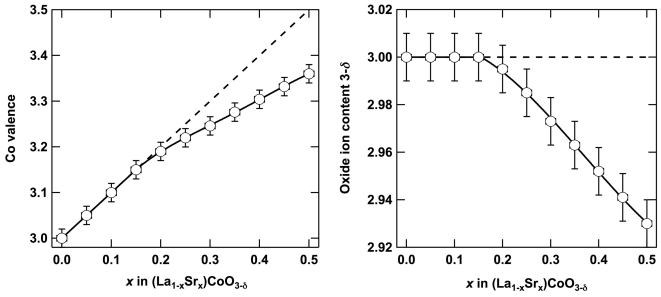

Fig. 2 (a) Co valence estimated by potentiometric–titration (open circle) and calculated without oxide ion vacancies (broken line), and (b) oxide ion content calculated from Co valence as a function of x in $(La_{1-x}Sr_x)CoO_{3-\delta}$.

3 Results and discussion

3.1 Characterization, Co valence, and oxide ion content

XRD patterns revealed that all samples showed a single phase with a perovskite structure. All sample compositions were consistent with the nominal composition within measurement error by ICP.

The oxide ion content and the oxide ion site occupancy [g(O)] were calculated from Co valence (Z) estimated by potentiometric–titration measurements using Mohr's salt[22]. The relationship between Z and the oxide ion content is shown below:

$$\delta = \frac{3+x-Z}{2}, \quad (2)$$

where x is Sr content, and δ is oxide ion deficiency. Fig. 2 shows (a) Co valence and (b) the oxide ion content as a function of x. For $x \leq 0.15$, LSC is essentially stoichiometric ($\delta \approx 0$). For $x > 0.15$, δ increases with increase in x. There are many reports about Co valence and the oxide ion content estimated by various methods[10,16,18,34]. Our results of the tendency for Co valence and the oxide ion content as a function of x are similar to the previous studies[10,16,18,34]. g(O) for Rietveld refinements was calculated from the oxide ion content by the following equation:

$$g(O) = \frac{3-\delta}{3}. \quad (3)$$

3.2 Rietveld refinements

Figure 3 shows the result of Rietveld refinements with the observed SR-XRD and the calculated profile of $(La_{0.75}Sr_{0.25})$

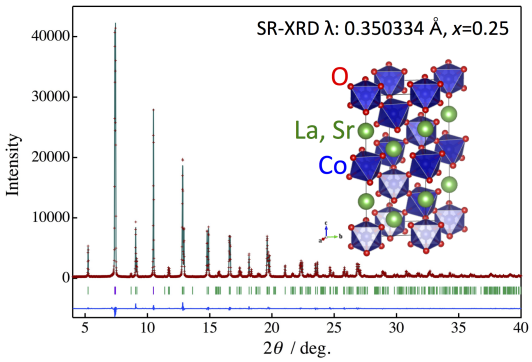

Fig. 3 Observed, calculated, and differential patterns of Rietveld refinements of synchrotron X-ray diffraction for $(La_{0.75}Sr_{0.25})CoO_{2.985}$. The brown plus symbols and the green line denote the observed and calculated intensities, respectively. Short verticals indicate the position of possible Bragg reflections of rhombohedral structure. The difference between the observed and calculated profiles is plotted at the bottom. The wavelength of the incident synchrotron X-ray is 0.350334 Å.

$CoO_{2.985}$. The inset of Fig. 3 presents the crystal structure of LSC with space group $R\bar{3}c$. The existence of an 113 reflection at a characteristic line at $2\theta = 8.68°$, *viz.*, $d_{113} = 2.31$ Å, in all SR-XRD patterns indicates that the crystal structure of all LSC samples belongs to the space group $R\bar{3}c$. Tables S3 and S4 list the positional data for analysis and the results of structural parameters along with the reliability factors (*R*-factors)†. *R*-factors, after Rietveld refinements of SR-XRD for LSC, are sufficiently small for discussing structural parameters in detail and performing MEM analysis.

3.2.1 Lattice parameters and Co–O bond length

Figure 4 (a) shows the lattice parameters as a function of x. The lattice parameter of the c–axis increase with increase in x. The a and b–axis, on the other hand, increases up to $x = 0.15$, and reduces for $x > 0.15$. The behavior of Co–O bond length in Fig. 4 (b) denotes the same tendency of the a and b–axis. The lattice parameters and Co–O bond length are in good agreement with those reported by Kozuka et al., Mineshige et al., and Iwasaki et al.[9,10,16,18]. Mineshige et al. discussed the correlation between the M–I transition and the decrease of Co–O bond length[10]. Kozuka et al. explained that Co–O bond length was associated with the effective mass and the spin transition[9]. It is well known that Co–O bond length reduces with increase in Co valence[35]. Therefore, the region for $x < 0.15$, in which Co–O bond length increases, is seen as an anomalous tendency reported by Kozuka et al., and Mineshige et al.[9,10]. This region is consistent with the semiconductive region, as reported in literature[9,10,16,18]. We suggest that the increase of the Co–O bond length is contributed by changing in

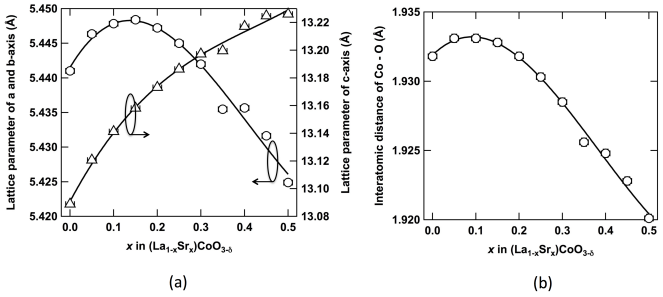

Fig. 4 (a) Lattice parameters of a, b, and c–axis, and (b) Co–O bond length as a function of x in $(La_{1-x}Sr_x)CoO_{3-\delta}$.

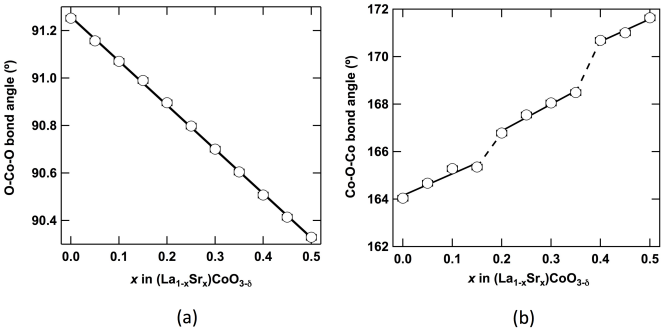

Fig. 5 (a) O–Co–O and (b) Co–O–Co bond angle as a function of x in $(La_{1-x}Sr_x)CoO_{3-\delta}$.

the spin configuration from the low spin (LS) to the intermediate spin (IS) and/or the high spin (HS) state. This supposition is discussed using XAS and FPC as shown later.

3.2.2 O–Co–O and Co–O–Co bond angle

Figures 5 (a) and (b) show x dependence of O–Co–O and Co–O–Co bond angle, respectively. The value of O–Co–O angle approaches 90° with increase in x. This result indicates that the symmetry of CoO_6 in LSC becomes higher rapidly with increase in x. Co–O–Co bond angles between CoO_6 hexahedrons in LSC approaches 180° with increase in x in Fig. 5 (b). Furthermore, we find discontinuous changes of Co–O–Co bond angles at $x = 0.15$ and 0.35. In particular, the composition $x = 0.15$ with this discontinuous change is in good agreement with that with changing the tendency of Co–O bond length and M–I transition. The correlation between Co–O–Co bond angle and x was reported in detail by Kozuka et al., Mineshige et al., and Mastin et al.[9,10,34]. They, however, did not find the discontinuous change of Co–O–Co bond angle. In contrast, it is possible to observe the discontinuous change of Co–O–Co bond angle since we estimated the parameters very precisely by Rietveld refinements using SR-XRD data in this work. It has been known that electrons are able to be itinerant

for increasing the overlap integrations between e_g orbitals of Co and σ and/or π bonds of oxide ion while Co–O–Co bond angle approach 180° [10,37,38,41,42]. We will attempt to discuss the correlation among Co–O–Co angle, σ_e, and $D_{O^{2-}}$ by using FPC in the later part.

3.2.3 Atomic displacement parameters

There are few reports discussing the atomic displacement parameter (U) of crystal structures. It is difficult to accurately estimate U by Rietveld refinements, because U correlates strongly with other parameters, *i.e.*, the site occupancies, the surface roughness, *etc*. Therefore, we evaluated the g(O) calculated from Co valence estimated using the potentiometric–titration [22]. Using high energy SR–XRD with a transmission method for Rietveld refinements, the anisotropic atomic displacement parameters (U_{aniso}), *i.e.*, U_{11}, U_{22}, U_{33}, U_{12}, U_{13}, and U_{23}, are able to be discussed. It is constrained for LSC with space group $R\bar{3}c$ that U_{22} and U_{13} are equal to U_{11} and U_{23}, respectively. Fig. 6 shows U_{aniso} of the cation sites as a function of x. U_{ii} of the cation sites varies significantly in $x \leq 0.15$. Meanwhile, U_{ij} of the cation sites is independent of x, and the values of U_{ij} are smaller than those of U_{ii}. The values of U_{33} of the cation sites are larger than those of U_{11} and U_{22} for $x \leq 0.15$. These phenomena mean that the cations disorder along the c–axis for $x \leq 0.15$. For $x > 0.20$, the values of U_{33} are equal to those of U_{11} and U_{22}, that is, U_{aniso} changes to the isotropic atomic displacement parameter (U_{iso}). The increased the symmetry with increase in x for LSC may cause the change from U_{aniso} to U_{iso} of the cation sites.

Figure 7 shows U_{aniso} of the oxide ion site as a function of x. The values of U_{33} are larger than those of U_{11} and U_{22} for the whole region. In other words, the disorder and/or the thermal vibration of the oxide ion toward the c–axis are larger than those toward the a and b–axis in LSC. Furthermore, the values of U_{ii} increase with increase in x for $x < 0.15$, reduce with increase in x for $0.15 \leq x < 0.30$, and become constant for $x \geq 0.3$. U_{aniso} of the oxide ion site would be deeply correlated to Co valence, oxide ion deficiency, structural parameters, and symmetry of LSC. For $x < 0.15$, the origin of increasing U_{aniso} would be increasing the rate of Co^{4+} by Sr substitution. On the other hand, the decreasing U_{aniso} for $x \geq 0.15$ may respond to become the higher symmetry with increase in x. For $x > 0.3$, the values of U_{aniso} become constant due to the combination of the next two effects. The first is that the becoming higher symmetry of LSC contributes to reduce the value of U_{aniso}. The second is that the values of U_{aniso} increase with increase in oxide ion deficiencies.

The values of $|U_{13}|$ and $|U_{23}|$ of the oxide ion site are larger than those of $|U_{12}|$ of this site. The direction of U_{13} and U_{23} of the oxide ion site are in the vertical direction of Co–O bond. This result consists with that of Yashima et al. using neutron diffraction [43,44]. The U_{13} and U_{23} in the vertical direction of Co–O bond would enhance the oxide ion migration to other oxide ion site [43,44].

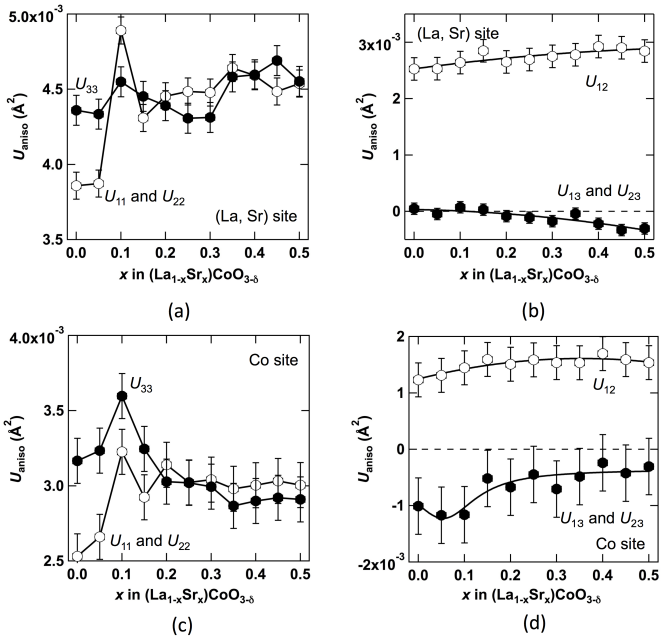

Fig. 6 Anisotropic atomic displacement parameter of cation sites, (a) U_{11}, U_{22}, and U_{33} of (La, Sr) site, (b) U_{12}, U_{13}, and U_{23} of (La, Sr) site, (c) U_{11}, U_{22}, and U_{33} of Co site, (d) U_{12}, U_{13}, and U_{23} of Co site as a function of x in $(La_{1-x}Sr_x)CoO_{3-\delta}$.

3.3 Electron density estimated by Maximum Entropy Method

MEM analysis is one of the methods for estimating electron density using experimental data [45,46]. Many studies discussed electron densities and disordered atoms in materials by MEM analysis using SR-XRD and neutron diffraction data [43,44,47–53]. In this present work, the electron density and the covalency at (La, Sr)–O and Co–O planes for LSC is discussed by MEM analysis. MEM analysis is performed using the structure parameters obtained from Rietveld refinements. Table S5 lists R-factors and full width at half maximum (FWHM) of $(|F_{MEM}|\text{-}|F_{obs}|)/\sigma_{obs}$ ($|F_{MEM}|$: structure factor calculated by MEM analysis, $|F_{obs}|$: observed structure factors, σ_{obs}: estimated standard uncertainty of observed structure factor)†. Fig. 8 (a) shows the correlation between frequency and $(|F_{MEM}|\text{-}|F_{obs}|)/\sigma_{obs}$ from the results of MEM analysis for $(La_{0.70}Sr_{0.30})CoO_{2.973}$. Gaussian functions are able to fit $(|F_{MEM}|\text{-}|F_{obs}|)/\sigma_{obs}$ of all MEM analysis. The values of R_W are 1.2139–1.4400, and the values of FWHM for $(|F_{MEM}|\text{-}|F_{obs}|)/\sigma_{obs}$ are 0.394815–0.796632 in Table S5† [49]. These informations are sufficient to qualify for further discus-

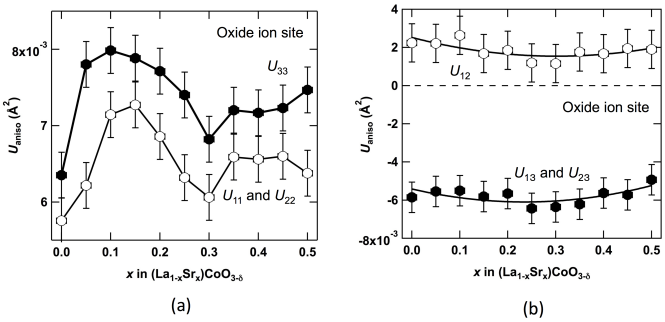

Fig. 7 Anisotropic atomic displacement parameter of oxide ion site, (a) U_{11}, U_{22}, and U_{33}, (b) U_{12}, U_{13}, and U_{23} as a function of x in $(La_{1-x}Sr_x)CoO_{3-\delta}$.

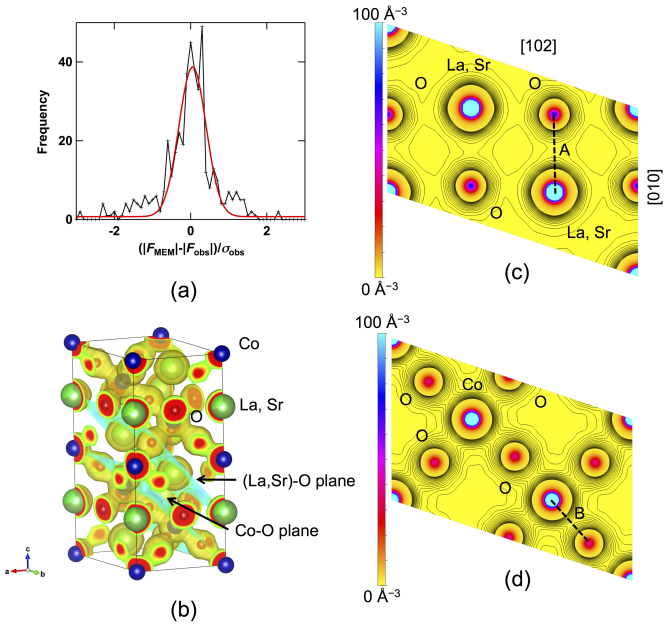

Fig. 8 (a) 3D electron density view for $x = 0.3$ with isosurface of 0.5 Å^{-3}, and Co–O and (La, Sr)–O plane with $(\bar{1}02)$. (b) Correlation between frequency and $(|F_{MEM}| - |F_{obs}|)/\sigma_{obs}$, and red line: fitted Gaussian function. Electron density distribution of (c) (La, Sr)–O and (d) Co–O planes for $x = 0.3$ with contour line: 0.3-2 Å^{-3}, step 0.1 Å^{-3}. Minimum electron density defined in A and B dashed line of (c) (La, Sr)–O and (d) Co–O planes.

sion on MEM electron densities for these system.

Figure 8 (b) shows the electron density for LSC ($x = 0.30$) with the isosurface 0.5 Å^{-3}, and (La, Sr)–O and Co–O planes of $(\bar{1}02)$. Figs. 8 (c) and (d) show the electron density map of (La, Sr)–O and Co–O planes, respectively. At a glance, it is clear that Co–O plane possesses higher covalencies and more isotropic bonds than (La, Sr)–O one.

We attempt to discuss the electron density of as a function of x. In particular, the minimum electron densities (MEDs), defined as the smallest electron density of A dashed line in (La, Sr)–O bond [Fig. 8 (c)] and B dashed line in Co–O bond [Fig. 8 (d)], are estimated. Fig. 9 shows MEDs of (La, Sr)–O and Co–O bonds. MED of Co–O bonds is higher than that of (La, Sr)–O bonds, and the difference between MEDs is large, *i.e.*, approximately $0.25 - 0.40$ Å^{-3}. MED of Co-O bonds in LSC are close to those of Co–O, Mn–O, Zr–O, and Nb–O bonds in perovskite oxide[47,48,52,53]. The results of MEDs indicate that Co–O and (La, Sr)–O bonds are covalent and ionic, respectively. In addition, Co–O planes with the high covalency would dominate σ_e and $D_{O^{2-}}$ more deeply than (La, Sr)–O planes. MED of (La, Sr)–O bond decreases with increase in x by reason of the substitution from La^{3+} to Sr^{2+}. In contrast, MED of Co–O bond increases slightly with increasing x for $x \leq 0.20$. The increased MED may enhance σ_e for $x \leq 0.20$. While MED of Co–O bond is saturated for $x > 0.30$, σ_e become constant for this region. From the results of MED of Co–O bond, the covalency of Co–O bond may be associated with σ_e. This tendency of MED is in agreement with that reported by Hanashima et al.[15].

3.4 X-ray absorption spectra

It is well known that a K–edge energy of XAS is strongly affected by a valence state. This relationship has been extensively studied for a number of transition metal perovskite oxides[35,54–59]. The normalized XANES spectra and pre–edge peaks of Co K–edge are shown in Figs. 10 (a) and (b), respectively. In this work, we do not discuss XANES, but pre–edge peaks, which is interpreted easily for $1s \rightarrow 3d$ and/or $4p$ transition.

3.4.1 Pre-edge spectra

The origin of the pre–edge peaks is due to the electric quadrupolar Co $1s \rightarrow 3d$ transition and/or dipolar Co $1s \rightarrow 4p$ hybridized with Co $3d$[60]. The hybridization between d and p orbitals is strictly regulated by the symmetry of the central Co atom in the CoO_6, and the existence of the p–character would affect pre–edge features, remarkably. The symmetry of Co species in all the present LSC samples is O_h. We assume that the pre–edge of Co is derived from the quadrupolar Co $1s \rightarrow 3d$ transition in this work. As mentioned above, the observation on the pre–edge, which is related to the Fermi level energy (E_F) and DOS at E_F, is worthwhile discussing the electronic structure and the spin configuration. Furthermore, the electronic structure and the spin configuration are deeply related to σ_e. The pre-edge peaks of Co perovskite oxide have been extensively studied in literature. Jiang et al. and Haas et al. investigated x dependence of the pre–edge peaks of Co atom in LSC. They, however, did not discuss quantitatively the

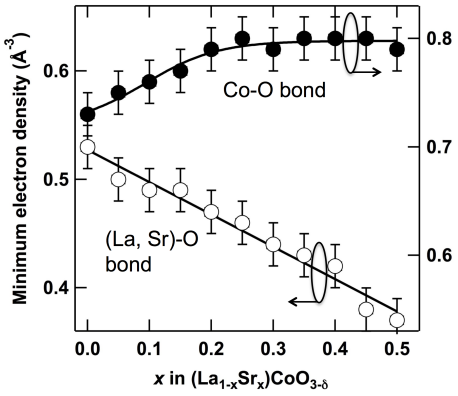

Fig. 9 Minimum electron density in (La, Sr)–O bond (open circle), and Co–O bond (closed circle) as a function of x in $(La_{1-x}Sr_x)CoO_{3-\delta}$.

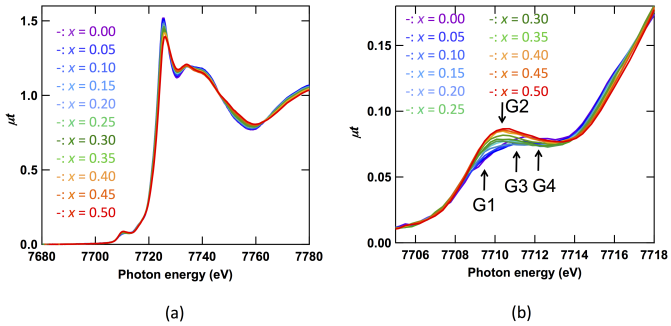

Fig. 10 (a) X–ray absorption near edge structure spectra and (b) pre–edge peaks at Co K–edge.

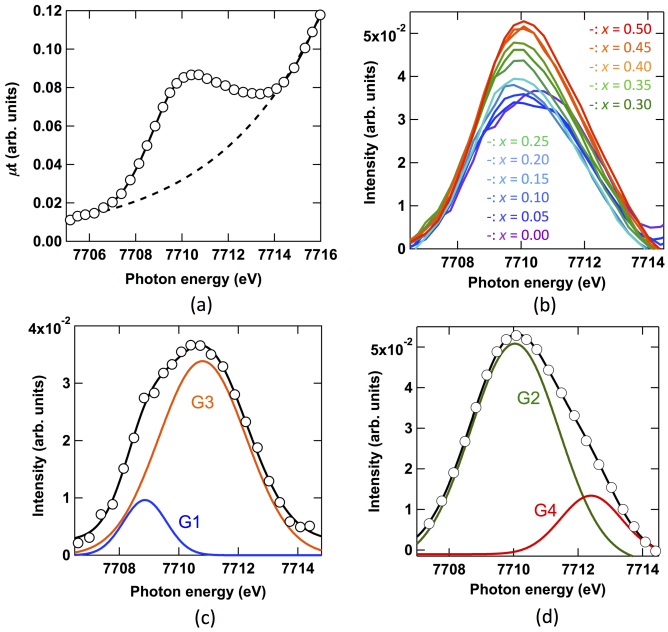

Fig. 11 (a) Pre–edge raw spectrum (open circle and solid line) of $LaCoO_3$ with background function (dashed line: Hill function). (b) Net intensity of pre–edge peaks removed background function as a function of x in $(La_{1-x}Sr_x)CoO_{3-\delta}$. (c) and (d) Net intensity of pre–edge spectrum of $LaCoO_{3.000}$ and $(La_{0.5}Sr_{0.5})CoO_{2.931}$, fitted by two Gaussian functions, open circle: net intensities, solid line: calculated intensities with two Gaussian functions, blue line: Gaussian function related to G1, orange line: Gaussian function related to G3, green line: Gaussian function related to G2, red line: Gaussian function related to G4.

correlation among the pre–edge peak, the band structure, and the spin configuration[56,61]. In this work, we analyze the pre–edge peaks by fitting with Gaussian functions, and establish the quantitative relation among the pre–edge peaks, the band structures, and the spin configurations.

Figure 10 (b) shows the enlarged view around the pre–edge peak. The pre–edge peaks of Co K–edge are composed of several peaks with their energies around 7709 eV (G1), 7710 eV (G2), 7711 eV (G3), and 7712 eV (G4) as shown in Fig. 10 (b). The Hill function is used as the background function for obtaining the net intensity of the pre–edge peak in Fig. 11 (a). The net intensity of the pre–edge peak was extracted from the raw pre–edge intensity in Fig. 11 (b). At a glance, the intensities and the positions of the pre–edge peaks increased and shifted to lower energy with increase in x, respectively. The increasing intensity of the pre–edge means that the hole is doped to d orbital, that is, this result is in agreement with x dependence of Co valence in Fig. 2 (b). With further inspection at the pre–edge peaks, we find that the pre–edge peaks are fitted by two Gaussian functions as shown in Figs. 11 (c) and (d). For $x < 0.15$, the pre–edge peaks are composed of the main (G3) and minor (G1) peaks around 7711 and 7709 eV, respectively. On the other hand, for $x \geq 0.15$, the pre–edge peak becomes broad and weak around 7712 eV (G4), while the peak (G2) around 7710 eV gets strong. In previous studies of Co pre–edge, the low energy peaks (G1, G2) and high energy peaks (G3, G4) have been thought to be contributed, respectively, by the transitions of $1s \rightarrow t_{2g}$ and $1s \rightarrow e_g$ [56,61–63].

The peak position, full width at half maximum (FWHM), peak area, and e_g/t_{2g} area ratio are estimated from the fitting pre–edge with two Gaussian functions as shown in Figs. 12 (a), (b), (c), and (d). Fig. 12 (a) shows x dependence of the peak position energy of each Gaussian function as a function of x. For $x < 0.15$, G1 and G3 peaks position energies are around 7709 and 7711 eV, respectively, and remained virtually constant. The difference of peak positions between G1 and G3 peak is approximately 2 eV for $x < 0.15$. For $x \geq 0.15$,

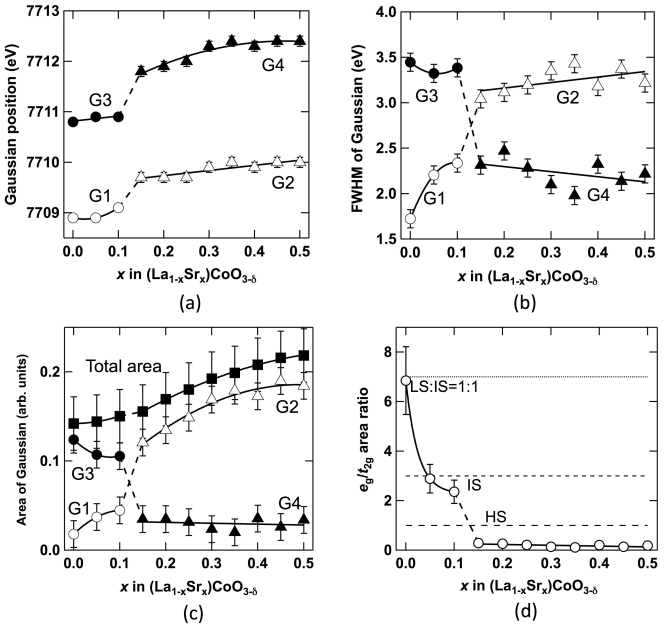

Fig. 12 (a) Pre–edge peak energies of G1, G2, G3, and G4 as a function of x in $(La_{1-x}Sr_x)CoO_{3-\delta}$. (b) Full width at half maximum of G1, G2, G3, and G4 as a function of x in $(La_{1-x}Sr_x)CoO_{3-\delta}$. (c) Area of pre–edge peak and G1, G2, G3, and G4 as a function of x in $(La_{1-x}Sr_x)CoO_{3-\delta}$. (d) e_g/t_{2g} area ratio of area as a function of x in $(La_{1-x}Sr_x)CoO_{3-\delta}$.

G2 and G4 peak position energies are around 7710 and 7712 eV, and these energies increased slightly with increase in x. The energy difference between G2 and G4 peak positions is greater than that for $x < 0.15$. This means that the symmetry becomes higher with increasing x for $x < 0.15$.

Figure 12 (b) shows x dependence of FWHM of each fitted Gaussian function. For $x < 0.15$, FWHM of G3 peak is about twice larger than that of G1 peak, and remaines virtually unchanged. By contrast, FWHM of G1 peak increases dramatically with increase in x. For $x \geq 0.15$, FWHM of G2 peak is larger than that of G4 peak, although FWHMs of both peaks remain virtually unaltered. These results suggest that the band width of t_{2g} is larger than that of e_g for $x \geq 0.15$.

Figure 12 (c) shows x dependence of the area of each fitting Gaussian function as well as the total area of two peaks. For $x < 0.15$, the area of G3 peak is larger than that of G1 peak, and decreases with increase in x. On the other hand, that of G1 peak increases with increasing x. The area of G3 peak decreases dramatically at $x = 0.15$, and that of G4 peak maintains constant with increasing x for $x \geq 0.15$. On the contrary, the area of G2 peak increases and is gradually saturated with increasing x for $x \geq 0.15$. For $x \geq 0.15$, the dependence of the total pre–edge area is similar to that of Co valence, that is, this phenomenon supports our presumption of relating between Co valence and the pre–edge. These results indicate that the hole is doped to t_{2g} state, and the spin state changes from LS to HS state.

Figure 12 (d) shows e_g/t_{2g} ratio (e_g: G3 and G4 and t_{2g}: G1 and G2) of area as a function of x, and this analysis is preferred by Medarde et al[64]. These results suggest that the spin states for $x < 0.05$ are a mixed LS and IS state whereas for $0.05 \leq x < 0.15$, the spin states are IS. On the other hand, for $x \geq 0.15$, the spin states are HS with x dependence of e_g/t_{2g} area rate decreases with increase in x.

Fig. 13 shows the number of t_{2g} (open circle), e_g (closed circle), and $3d$ total electrons (closed square) as a function of x in the ionic (a) and covalent (b) models. This analysis follows the method proposed by Medarde et al[64]. The total number of $3d$ electrons was calculated with considering the oxide ion vacancy estimated by the potentiometric–titration. The electron number of t_{2g} is larger than that of e_g for the ionic (a) and covalent (b) models in $x < 0.15$. By contrast, this relationship gets the opposite tendency for $x \geq 0.15$. Actually, the spin configuration of LSC would be combination of the ionic and the covalent models. The model may be ionic one for $x < 0.15$, and covalent for $x \geq 0.15$.

From the results of the pre–edge analysis, it is speculated that the spin configurations are contributed by LS and/or IS state for $x < 0.15$ whereas it is by the contribution from the HS for $x \geq 0.15$. The difference in the spin configurations between $x < 0.15$ and $x \geq 0.15$ would be associated with σ_e and M–I transition. Especially, the transition from LS to HS state involves the increase of the electron number of e_g, *e.g.*, $d_{x^2-y^2}$ and $d_{3z^2-r^2}$. As a result, the covalency of Co–O bond increases, and the behavior of σ_e is metallic for $x \geq 0.15$. Kozuka et al. reported that HS state had a higher mobility than LS one[16]. The pre-edge analysis in this work is in good agreement with their concept, and we confirmed the spin transition from LS to HS state at $x = 0.15$ to occur concomitantly with M–I transition.

3.5 Density of states calculated by the first principles calculations

The structural parameters with high accuracy and precision were able to be obtained by Rietveld refinements using SR-XRD data. These structural parameters, *viz.*, lattice parameters and Co–O–Co bond angles, are used as input parameters in FPC to understand the influence of the change of structural parameters on σ_e. Co–O–Co bond angle is changed by changing the oxide ion site fractional coordinate [x(O)] in FPC. In this work, the structure model of $LaCoO_3$ with space group $R\bar{3}c$ is used for FPC. We are able to study more precisely the influence of the structural parameters than that caused by the hole doping during Sr substitution. Table S1 lists the condi-

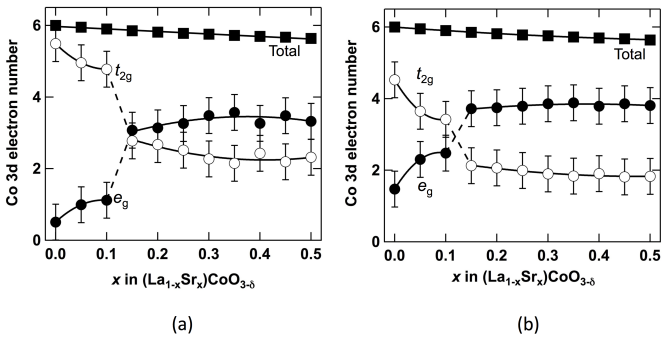

Fig. 13 Electron number of t_{2g} (open circle), e_g (closed circle), and 3d total electron (closed square) as a function of x in the (a) ionic and (b) covalent model with oxide ion vacancies.

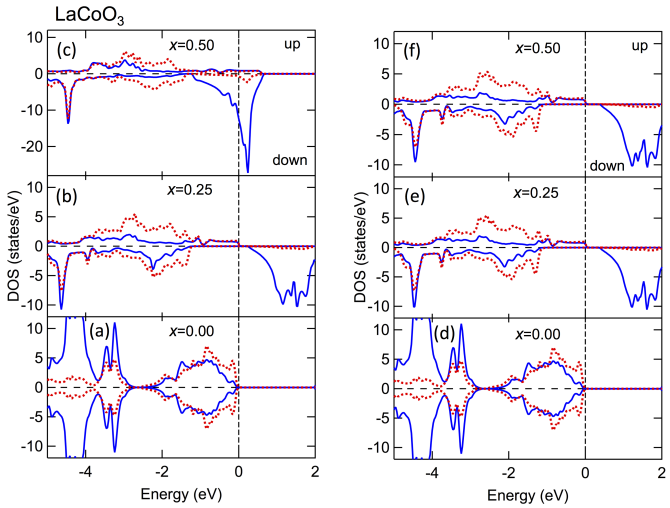

Fig. 14 Density of states of Co (solid line) and oxide ion (broken line) for $LaCoO_3$ estimated by first principle calculations. (a), (b), and (c) using the lattice parameters and bond angles of x =0.00, 0.25, and 0.50, respectively. (d), (e), and (f) using only the lattice parameters of x =0.00, 0.25, and 0.50, respectively.

tions of FPC†. Figs. 14 shows DOS for $LaCoO_3$ calculated with GGA+U method. DOS in Figs. 14 (a), (b), and (c) are calculated with varying Co–O–Co bond angles and lattice parameters. Figs. 14 (a), (b), and (c) are the results using the lattice parameters and bond angles of x =0.00, 0.25 and 0.50, respectively. These DOS are compared with those in Figs. 14 (d), (e), and (f) which are calculated with using only the lattice parameters of x =0.00, 0.25 and 0.50, respectively. LS state model is used to FPC in Figs. 14 (a) and (d). Kozuka et al. reported that DOS of $LaCoO_3$ which was calculated with LS state model. The results in Figs. 14 (a) and (d) is consistent with the result of Kozuka et al.[16].

From results of the pre–edge analysis, HS state model of FPC for $x \leq 0.15$ is preferred than LS state model in Figs. 14 (b), (c), (e), and (f). DOS in Fig. 14 (b) has a tail near E_F, and DOS of Co 3d with the down spin comes down to E_F. These results are slightly different from those of Kozuka et al.[16]. Because we did not consider Sr doping to La site in FPC. DOS, which was considered the change of Co–O–Co bond angle, has smaller band gap than that unconsidered. Each band gap, considered and unconsidered the change of the bond angle, is 0.16 and 0.36 eV. Kozuka et al. reported that Co–O–Co bond angle did not enhance σ_e[9]. Meanwhile, the effect of Co–O–Co bond angle on σ_e is able to be observed, and the results in this work are consistent with the general assumptions[41,42]. By using HS model in Fig. 14 (c) with structural parameters of $x = 0.50$, we observe increase in DOS of Co 3d near E_F. The result, however, considered only lattice parameter, does not exhibit DOS at E_F. Figs. 14 (c) and (f) show the effect of Co–O–Co band angle. DOS near E_F of Fig. 14 (c) contains mainly e_g, *e.g.*, $d_{x^2-y^2}$ and $d_{3z^2-r^2}$, and this DOS has narrow band width. This result is in good agreement with that of FWHM for the pre–edge analysis.

3.6 Correlation between the electron conductivity and the band structure

It is discussed the correlation between σ_e and the band structure using the corresponding results of structural parameters, electron densities, pre–edge analysis, and FPC. In particular, we focus on the band structure of $x < 0.15$ and $x \geq 0.15$ with semiconductive and metallic behaviors, respectively. For $x < 0.15$, the spin configuration changes from LS to IS and/or HS state with increase in x, as is able to be appreciated from the following results. Co–O bond length and Co–O–Co bond angle increase with x, and the electron number of t_{2g} is higher than that of e_g. Furthermore, the results of FPC in Figs. 14 (a) and (d) explain σ_e of $x = 0.00$. The band structure of $x = 0.00$ has a clear band gap of approximately 2 eV. The results of XAS and FPC indicate that t_{2g} electrons for $LaCoO_3$ localize because of the narrow width of FWHM for the pre–edge and DOS. The correlation between the width of DOS and elective mass (m^*) is shown in next equation,

$$\frac{1}{m^*} = \frac{1}{\hbar^2}\frac{d^2\varepsilon}{dk^2} \quad (4)$$

where $\hbar$ is Planck's constant, ε is energy of free electron, k is wave number. Equation (4) reveals that the narrow width of DOS results in a heavy m^*, that is, low mobility and σ_e. Therefore, σ_e of $LaCoO_3$, which has the heavy m^* and the large band gap, is small[16,18].

From results of the pre–edge analysis, the spin transition from LS to HS state occurs for $0.05 < x \leq 0.15$, that is, the

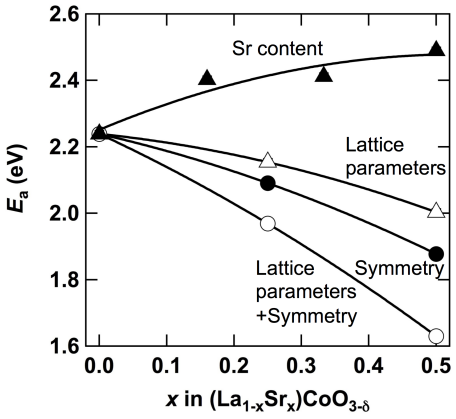

Fig. 15 Activation energy (E_a) of oxide ion diffusion estimated by first principle calculations. Parameters of FPC are lattice parameters and x(O) of oxide ion site fractional coordinate (open circle), x(O) (closed circle), lattice parameters (open triangle), and Sr content (closed triangle).

electron numbers of e_g, *e.g.*, $d_{x^2-y^2}$ and $d_{3z^2-r^2}$, increase with increase in x. These results of the spin transition are in agreement with the increase of Co–O bond length for $x < 0.15$, and the increasing covalency of Co–O bond for $x \leq 0.2$. The angle between CoO_6 hexahedrons gets close to 180°, so that the tailed DOS at E_F, which means lightweight m^*, is generated. From results of the pre–edge analysis and FPC for $x > 0.3$, the width of DOS is narrow indicating m^* becomes heavy, and the spin configuration and the covalency of Co–O bond dose not change significantly. These results and ideas relate to the metallic behavior and the saturation of σ_e for $x > 0.3$.

3.7 Oxide ion diffusion studied by first principles calculations

It is well known that $D_{O^{2-}}$ increases with increasing Sr content[20]. Recently, there are many studies for ion migration using FPC[68,69]. In this work, $D_{O^{2-}}$ is investigated by FPC with varying the condition of calculations, *viz.*, lattice parameter, the symmetry as O–Co–O and/or Co–O–Co bond angle, and Sr content. The structural parameters were estimated by Rietveld refinements using SR-XRD data. Table S2 lists the conditions of FPC†. Fig. 15 shows E_a for $D_{O^{2-}}$. It is expected that E_a would be reduced with increase in Sr content because the covalency of (La, Sr)–O bond decreased with increase in x. We, however, got the opposite results about E_a estimated by FPC as a function of x. The covalency of (La, Sr)–O bond is not related to $D_{O^{2-}}$. On the other hand, the change of lattice parameters and the symmetry affect E_a. Specifically, the effect on E_a of the changing symmetry is higher than that of lattice parameters. E_a decreases with becoming higher the symmetry of LSC. The effect of the symmetry is consistent with the results of Islam estimated by molecular dynamics techniques[21]. As for the lattice parameters, the increased unit cell volume with increasing x may make E_a reduced. It is speculated that the oxide ion diffusion space increases with increasing the unit cell volume, so that E_a decreases. The effect of lattice parameters, however, decreases to reduce E_a with increasing x because of the saturation of increased unit cell volume for $x > 0.4$. We find that the importance for reducing E_a is not Sr substitution but structural parameters, *e.g.*, lattice parameters, and symmetry of CoO_6 in LSC.

4 Conclusion

MIEC mechanism of $(La_{1-x}Sr_x)CoO_{3-\delta}$ (LSC) ($x = 0.00 - 0.50$) was investigated experimentally by Rietveld refinements, MEM analysis, XAS analysis, and verified by FPC. The LSC samples were prepared by the solid state reaction, followed by annealing at 673 K and 48 h in air to ensure that the samples were essentially in their controlled stoichiometric compositions. Co valence and g(O) of LSC were estimated by the potentiometric–titration using Mohrs salt for a detailed discussion of Rietveld refinements and XAS analysis. No significant δ was generated for $x \leq 0.15$. Meanwhile, δ was formed and increased with increase in Sr content for $x > 0.15$. At $x = 0.15$, the change of the behavior for σ_e from semiconductor to metallic accompanied by the spin transition from LS to HS state which was confirmed by the pre–edge analysis. In addition, the covalency of Co–O bond increased with an increase in x for $x \leq 0.20$. Concerning structural parameters, Co–O–Co bond angle approached to 180 °, and had a discontinuous change at $x = 0.15$. The results of FPC demonstrated that Co–O–Co bond angle play an important role to change of DOS. For these results, Co–O–Co bond angle may cause the spin transition, and make the covalency of Co–O bond enhanced so that σ_e increase. For $x > 0.30$, σ_e was saturated in this region, the spin state and the covalency of Co–O bond did not change significantly.

As for $D_{O^{2-}}$, we discussed the correlation between structural parameters and $D_{O^{2-}}$, and verified this correlation by using FPC. A large U_{aniso} of the oxide ion site, which was in the vertical direction of Co–O bond, was observed by using Rietveld refinements, and helps the oxide ion migrate in consequence. It was concluded that the main reason for reducing E_a of $D_{O^{2-}}$ is not Sr substitution but the lattice parameters and the symmetry of LSC. Especially, the high symmetry of LSC is more effective to decrease E_a of $D_{O^{2-}}$ than the lattice parameters.

In this work, we presented here a comprehensive relation among MIEC mechanism for LSC, their structural parameters, electron densities, spin configurations and band structures, empirically and theoretically.

Acknowledgements

We thank Dr. F. Izumi of Nagoya Institute of Technology and Dr. K. Momma of National Museum of Nature and Science for their assistance with the RIETAN-FP, Dysnomia, and VESTA computer programs, which allowed us to perform Rietveld refinements, MEM analysis, and 3D visualization of the considered samples, respectively. We are also grateful to Prof. T. Yamamoto of Waseda university and Mr. S. Yajima of AGCSeimichemical for the first principles calculations technique. Synchrotron X-ray experiments at the BL19B2 and BL14B2 beamline at SPring-8 were performed under Program No. 2008A1780, 2008B1896, 2010A1696, and 2011B1764, and we thank Dr. K. Osaka, Dr. T. Honma, and Ms. S. Hirayama for supporting experiments.

References

1 S. Singhal, Solid State Ionics 135 (2000) 305–313.
2 J. W. Stevenson, T. R. Armstrong, R. D. Carneim, L. R. Peederson, W. J. Weber, J. Electrochem. Soc. 143 (1996) 2722–2729.
3 S. C. Singhal, K. Kendal, High Temperature and Solid Oxide Fuel Cells, Elsevier Science, Amsterdam, 2003.
4 Perovskite Oxide for Solid Oxide Fuel Cells, Springer, New York, 2009.
5 V. Neburchilov, H. Wang, J. J. Martin, W. Qu, J. Power Sources 195 (2010) 1271–1291.
6 P. Hjalmarsson, M. Søgaard, A. Hagen, M. Mogensen, Solid State Ionics 179 (2008) 636–646.
7 D. J. L. Brett, A. Atkinson, N. P. Brandon, S. J. Skinner, Chem. Soc. Rev. 37 (2008) 1568–1578.
8 E. Y. Konysheva, S. M. Francis, J. T. S. Irvine, A. Rolle, R.-N. Vannier, J. Mater. Chem. 21 (2011) 15511–15520.
9 H. Kozuka, K. Yamagiwa, K. Ohbayashi, K. Koumoto, J. Mater. Chem. 22 (2012) 11003–11005.
10 A. Mineshige, M. Inaba, T. Yao, Z. Ogumi, J. Solid State Chem. 121 (1996) 423–429.
11 Y. Onose, Y. Tokura, Phys. Rev. B 73 (2006) 174421–174425.
12 Y. Kashiwada, H. Fujishiro, Y. Fujine, M. Ikebe, J. Hejtmanek, Physica B 378–380 (2006) 529–531.
13 A. Petrov, O. Kononchuk, A. Andreev, V. Cherepanov, P. Kofstad, Solid State Ionics 80 (1995) 189 – 199.
14 H. Takahashi, F. Munakata, M. Yamanaka, Phys. Rev. B 57 (1998) 15211–15218.
15 T. Hanashima, N. Shimizu, K. Yamawaki, S. Sasaki, Jpn. J. Appl. Phys. 46 (2007) 988–994.
16 H. Kozuka, H. Yamada, T. Hishida, K. Yamagiwa, K. Ohbayashi, K. Koumoto, J. Mater. Chem. 22 (2012) 20217–20222.
17 O. Toulemonde, N. N'Guyen, F. Studer, J. Solid State Chem. 158 (2001) 208–217.
18 K. Iwasaki, T. Ito, T. Nagasaki, Y. Arita, M. Yoshino, T. Matsui, J. Solid State Chem. 181 (2008) 3145–3150.
19 J. Mizusaki, Y. Mima, S. Yamauchi, K. Fueki, H. Tagawa, J. Solid State Chem. 80 (1989) 102–111.
20 A. Berenov, A. Atkinson, J. Kilner, E. Bucher, W. Sitte, Solid State Ionics 181 (2010) 819–826.
21 M. Saiful Islam, J. Mater. Chem. 10 (2000) 1027–1038.
22 Y. Idemoto, T. Kashima, N. Kitamura, Electrochemistry 80 (2012) 791–799.
23 K.Osaka, T. Matsumoto, K. Miura, M. Sato, I. Hirosawa, Y. Watanabe, AIP Conf. Proc. 1234 (2010) 9–12.
24 F. Izumi, K. Momma, Solid State Phenom. 130 (2007) 15–20.
25 F. Izumi, T. Ikeda, Mater. Sci. Forum. 321-324 (2000) 198–205.
26 F. Izumi, K. Momma, Mater. Sci. Eng. 18 (2011) 022001–022006.
27 F. Izumi, K. Momma, Z. Kristallogr., Proc. 1 (2011) 195–200.
28 K. Momma, F. Izumi, J. Appl. Crystallogr. 44 (2011) 1272–1276.
29 B. Ravel, M. Newville, J. Synchrotron Rad. 12 (2005) 537–541.
30 M. Newville, J. Synchrotron Rad. 8 (2001) 322–324.
31 K. Schwarz, P. Blaha, G. Madsen, Comput. Phys. Commun. 147 (2002) 71–76.
32 J. P. Perdew, K. Burke, M. Ernzerhof, Phys. Rev. Lett. 77 (1996) 3865–3868.
33 M. A. Korotin, S. Y. Ezhov, I. V. Solovyev, V. I. Anismov, D. I. Komskii, G. A. Sawatzky, Phys. Rev. B 54 (1996) 5309–5316.
34 J. Mastin, E. M-A, T. Grande, Chem. Mater. 18 (2006) 6047–6053.
35 Y. Orikasa, T. Ina, T. Nakao, A. Mineshige, K. Amezawa, M. Oishi, H. Arai, Z. Ogumi, Y. Uchimoto, J. Phys. Chem. C 115 (2011) 16433–16443.
36 J. A. Alonso, M. J. Martnez-Lope, C. de la Calle, V. Pomjakushin, J. Mater. Chem. 16 (2006) 1555–1560.
37 J. B. Torrance, P. Lacorre, A. I. Nazzal, E. J. Ansaldo, C. Niedermayer, Phys. Rev. B 45 (1992) 8209–8212.
38 S. R. Barman, A. Chainani, D. D. Sarma, Phys. Rev. B 49 (1994) 8475–8478.
39 M. A. Senaris-Rodriguez, J. B. Goodenough, J. Solid State Chem. 118 (1995) 323–336.
40 Y. Tokura, Y. Okimoto, S. Yamaguchi, H. Taniguchi, Phys. Rev. B 58 (1998) R1699–R1702.
41 J. L. Garcia-Munoz, J. Rodriguez-Carvajal, P. Lacorre, J. B. Torrance, Phys. Rev. B 46 (1992) 4414–4425.
42 P. G. Radaelli, D. E. Cox, M. Marezio, S.-W. Cheong, P. E. Schiffer, A. P. Ramirez, Phys. Rev. Lett. 75 (1995) 4488–4491.
43 M. Yashima, T. Tsuji, J. Appl. Crystallogr. 40 (2007) 1166–1168.
44 M. Yashima, T. Kamioka, Solid State Ionics 178 (2008) 1939 – 1943.
45 M. Sakata, M. Sato, Crystallogr. A 46 (1990) 263–270.
46 D. M. Collins, Nature 298 (1982) 49–51.
47 T. Itoh, Y. Nishida, A. Tomita, Y. Fujie, N. Kitamura, Y. Idemoto, K. Osaka, I. Hirosawa, N. Igawa, Solid State Commun. 149 (2009) 41–44.
48 T. Itoh, S. Shirasaki, Y. Fujie, N. Kitamura, Y. Idemoto, K. Osaka, H. Ofuchi, S. Hirayama, T. Honma, J. Alloys Compd. 491 (2010) 527–535.
49 T. Itoh, T. Hirai, J. Yamashita, S. Watanabe, E. Kawata, N. Kitamura, Y. Idemoto, N. Igawa, Physica B 405 (2010) 2091–2096.
50 Y. Idemoto, R. Muroi, N. Kitamura, T. Itoh, J. Am. Cream. Soc. 95 (2012) 3906–3911.
51 Y. Idemoto, T. Ito, N. Kitamura, T. Itoh, J. Phys. Chem. Solids 73 (2012) 1223–1228.
52 Y. Kuroiwa, H. Fujiwara, A. Sawada, S. Aoyagi, E. Nishibori, M. Sakata, M. Takata, H. Kawaji, T. Atake, Jpn. J. Appl. Phys. 43 (2004) 6799–6802.
53 C. Moriyoshi, J. Kato, Y. Terado, S. Wada, M. Takata, Y. Kuroiwa, J. Appl. Phys. 47 (2008) 7745–7748.
54 T. Itoh, S. Shirasaki, H. Ofuchi, S. Hirayama, T. Honma, M. Makayama, Solid State Commun. 152 (2012) 278–283.
55 T. Itoh, M. Nakayama, J. Solid State Chem. 192 (2012) 38–46.
56 O. Hass, C. Ludwig, U. Bergmann, R. N. Singh, A. Braun, T. Graule, J. Solid State Chem. 184 (2011) 3163–3171.
57 A. Deb, J. M. Ralph, F. J. Cairns, U. Bergmann, Phys. Rev. B 73 (2006) 115114–115123.
58 O. Hass, U. F. Vogt, C. Soltmann, A. Braun, W. S. Yoon, X. Q. Yang, T. Graule, Mater. Res. Bull. 44 (2009) 1397–1404.
59 N. Sundaram, Y. Jiang, I. E. Anderson, D. P. Belanger, C. H. Booth,

F. Bridges, J. F. Mitchell, T. Proffen, H. Zheng, Phys. Rev. B 102 (2009) 026401–026403.
60 T. Yamamoto, X-Ray Spectrometry 37 (2008) 572–584.
61 Y. Jiang, F. Bridges, N. Sundaram, D. P. Belanger, I. E. Anderson, J. F. Mitchell, H. Zheng, Phys. Rev. B 80 (2009) 144423–144437.
62 G. Vankó, J.-P. Rueff, A. Mattila, Z. Németh, A. Shukla, Phys. Rev. B 73 (2006) 024424–024433.
63 O. Haas, R. P. W. J. Struis, J. M. McBreen, J. Sold State Chem. 177 (2004) 1000–1010.
64 M. Medarde, C. Dallera, M. Grioni, J. Voigt, A. Podlesnyak, E. Pomjakushina, K. Conder, T. Neisius, O. Tjernberg, S. Barilo, Phy. Rev. B 73 (2006) 054424–054429.
65 P. Ravindran, P. Korzhavyi, H. Fjellvå g, A. Kjekshus, Phys. Rev. B 60 (1999) 16423–16434.
66 P. Ravindran, H. Fjellvåg, A. Kjekshus, P. Blaha, K. Schwarz, J. Luitz, J. Appl. Phys. 91 (2002) 291–303.
67 S. Medling, Y. Lee, H. Zheng, J. Mitchell, J. Freeland, B. Harmon, F. Bridges, Phys. Rev. Lett. 109 (2012) 157204–157208.
68 R. Merkle, Y. A. Mastrikov, E. A. Kotomin, M. M. Kuklja, J. Maiera, J. Electrochem. Soc. 159 (2012) B219–B226.
69 I. Kagomiya, K. Jimbo, K.-i. Kakimoto, M. Nakayama, O. Masson, Phys. Chem. Chem. Phys. 16 (2014) 10875–10882.